Mon. Not. R. Astron. Soc. **000**, 000–000 (0000) Printed 3 January 2022 (MN LATEX style file v2.2)

Simultaneous Millimeter-wave and X-ray monitoring of the Seyfert Galaxy NGC 7469

Ehud Behar[1⋆], Shai Kaspi[2], Gabriel Paubert[3], Nicolas Billot[4], Uria Peretz[1]
Ranieri D. Baldi[5,6], Ari Laor[1], Jelle Kaastra[7], Missagh Mehdipour[7]
[1] *Department of Physics, Technion 32000, Haifa 32000, Israel*
[2] *Wise Observatory and School of Physics and Astronomy, Tel Aviv University, Tel Aviv 69978, Israel*
[3] *Instituto de Radioastronoma Milimtrica, Avda. Divina Pastora 7, Ncleo Central, E-18012 Granada, Spain*
[4] *Observatoire Astronomique de l'université de Genève, 51 Chemin des Maillettes, 1290 Versoix, Switzerland*
[5] *School of Physics and Astronomy, University of Southampton, UK*
[6] *Dipartimento di Fisica, Universit degli Studi di Torino, via Pietro Giuria 1, I-10125 Torino, Italy*
[7] *SRON Netherlands Institute for Space Research, Sorbonnelaan 2, 3584 CA Utrecht, The Netherlands*

arXiv:1911.04544v1 [astro-ph.HE] 11 Nov 2019

3 January 2022

ABSTRACT

We report on daily monitoring of the Seyfert galaxy NGC 7469, around 95 GHz and 143 GHz, with the IRAM 30 m radio telescope, and with the *Swift* X-Ray and UV/Optical telescopes, over an overlapping period of 45 days. The source was observed on 36 days with IRAM, and the flux density in both mm bands was on average ~ 10 mJy, but varied by $\pm 50\%$, and by up to a factor of 2 between days. The present IRAM variability parameters are consistent with earlier CARMA monitoring, which had only 18 data points. The X-ray light curve of NGC 7469 over the same period spans a factor of 5 in flux with small uncertainties. Similar variability in the mm-band and in the X-rays lends support to the notion of both sources originating in the same physical component of the AGN, likely the accretion disk corona. Simultaneous monitoring in eight UV/optical bands shows much less variability than the mm and X-rays, implying this light originates from a different AGN component, likely the accretion disk itself. We use a tentative 14 day lag of the X-ray light curve with respect to the 95 GHz light curve to speculate on coronal implications. More precise mm-band measurements of a sample of X-ray-variable AGN are needed, preferably also on time scales of less than a day where X-rays vary dramatically, in order to properly test the physical connection between the two bands.

Key words: Galaxies: active – Galaxies: nuclei – galaxies: jets – radio continuum: galaxies – X-rays: galaxies

1 INTRODUCTION

Radio loud (RL) active galactic nuclei (AGN) are known to have relativistic jets on various scales, from pc to Mpc. On the other hand, radio emission from radio quiet (RQ) AGN is several orders of magnitude weaker, and has several possible origins. The implied high brightness temperature of these sources strongly suggests the presence of hot, non-thermal electrons, but the actual physical origin and location of the radio source in RQ AGN is still in debate. The nature of radio emission from RQ AGN could be due to weak jets, nuclear star formation, an AGN wind, or accretion-disk magnetic (i.e., coronal) activity. For a recent review see Panessa et al. (2019). Some VLBI images (Anderson et al. 2004; Ho & Peng 2001; Lal et al. 2004; Ulvestad et al. 2005) indicate source angular sizes as small as mas, or pc-scales for nearby sources, which can still be consistent with all of the above origins. Since these radio sources could be smaller than our contemporary imaging capability, one needs to revert to spectroscopy and timing in the attempt to characterize their physical origin.

1.1 Spectra

The radio spectra of RQ AGN have not been explored much. Recently, Laor et al. (2019) studied the spectral slope of 25 PG quasars (Schmidt & Green 1983) between 5 and 8.5 GHz, finding that a steep spectral slope of the flux den-

⋆ E-mail: behar@physics.technion.ac.il

sity $F_\nu \propto \nu^\alpha$ with $\alpha < -0.5$ occurs in highly accreting quasars with $L/L_{\rm Edd} > 0.3$, while flatter slopes of $\alpha > -0.5$ occur in quasars with $L/L_{\rm Edd} < 0.3$. The steep slope is typical of optically-thin synchrotron and was associated with an AGN wind, while a flat spectrum is indicative of an optically-thick source, and was associated with a compact AGN core. More generally, since the sources are non-thermal and the emission is likely due to synchrotron, observing at a few GHz limits the size of an opaque synchrotron source one has a chance to resolve, either angularly, or temporally. Synchrotron self-absorption at a few GHz makes a source of $L_\nu \sim 10^{30}$ erg s^{-1}Hz^{-1} opaque at the pc scales (e.g., Eq. 19 in Laor & Behar 2008). Hence, smaller scales are physically impossible to observe. Luckily, the synchrotron absorption coefficient α_ν decreases strongly with frequency ($\propto \nu^{-3}$), and thus the physical size of an opaque source decreases as well ($\propto \nu^{-5/4}$, Laor & Behar 2008). Consequently, observations at increasingly higher frequencies have the potential to reveal smaller structures close-in to the center of the AGN. This effect is further enhanced by the improved angular resolution with ν of the telescopes.

Above 300 GHz (sub-mm), the AGN spectrum rises steeply due to thermal dust emission (Barvainis et al. 1992; Hughes et al. 1993). Thus, the band between 30–300 GHz (crudely referred to here as the mm band) is the sweet spot in which one might be able to observe nuclear activity. This potential of observations around 100 GHz has led to several mm-wave campaigns of RQ AGN. Doi et al. (2005, 2011) observed a sample of low luminosity AGN and early type galaxies, both RQ and RL. 100 GHz (3 mm) fluxes of X-ray selected RQ AGN measured with ATCA and CARMA (Behar et al. 2015, 2018) indicate a spectral turnover between the cm and the mm bands. This distinct mm-wave spectral component appears superimposed on a steep spectrum of the more extended (optically thin) low-frequency source (perhaps an outflow? see Laor et al. 2019). If this new spectral component is due to optically thick synchrotron, it could be the sign of a much smaller source than the likely extended few-GHz source. More comprehensive cm- to mm-wave spectra were recently obtained by Inoue & Doi (2018), who used JVLA and ALMA to clearly identify this component in NGC 985 and in IC 4329A. These authors modeled their spectra in terms of coronal magnetic activity arising only a few 10s of Schwarzschild radii from the central black hole. Earlier theoretical works have explored the viability of coronal emission from around and near the black bole (Field & Rogers 1993; Inoue & Doi 2014; Raginski & Laor 2016).

1.2 Variability

Weak variability at 8.5 GHz on time scales of a few days for low-luminosity RQ AGN (Anderson & Ulvestad 2005), and of months for luminous RQ quasars (Barvainis et al. 2005) has been detected. Variability of RQ AGN typically <50% at 5-15 GHz on a year time scale has also been detected (Neff & de Bruyn 1983; Wrobel 2000; Mundell et al. 2009). Falcke et al. (2001) found that RQ AGN are more variable than RL AGN except for blazars, and that low-luminosity RQ AGN are among the most variable radio sources, likely due to the small black-hole mass and size.

Systematic radio monitoring of RQ AGN cores is difficult, both due to the numerous observations required, and due to the faintness (∼mJy) of the sources, which necessitates large interferometers, or few-hour exposures with smaller telescopes each time, as we do here. The size of an optically thick self-absorbed synchrotron source at a few GHz being around a pc, further underlines the need for high-frequency (mm-wave) observations, and in particular monitoring.

Doi et al. (2011) found significant 3-mm variability within months in a few low-luminosity RQ AGN. The only long-term mm-wave monitoring of a RQ AGN is that of Baldi et al. (2015), who monitored NGC 7469 with CARMA at 95 GHz over a period of 70 days. The source varied ($\pm 3\sigma$ from the mean) by a factor of 2 within 4-5 days, unlike its long-term steadiness at 8.4 GHz (Pérez-Torres et al. 2009).

1.3 Connection to X-rays

X-rays in RQ AGN vary rapidly, particularly in Seyfert galaxies on time scales of hours and less (Markowitz & Edelson 2004), which indicates they come from small length scales (the corona, $\lesssim$ light-hours), close to the black hole. If the mm-wave emission comes from the same hot coronal electrons that produce the X-rays, the two bands would be physically correlated. In terms of luminosity, Laor & Behar (2008) used the PG quasar sample (Schmidt & Green 1983) to demonstrate that L_R and L_X are correlated and follow the well established $L_R/L_X \sim 10^{-5}$ correlation observed in coronally active cool stars (Güdel & Benz 1993). In terms of variability, the sole mm-wave monitoring campaign of Baldi et al. (2015) indicate the variability parameters of NGC 7469 at 95 GHz are similar to those of NGC 7469 in (non-simultaneous) archival X-ray data, only with much larger uncertainties. However, in order to truly test the connection between the mm-wave and X-ray sources of RQ AGN, simultaneous monitoring is essential. Diligent attempts at 5 and 8.5 GHz, either focus on more RL objects (Bell et al. 2011), or meet limited success in RQ ones (Jones et al. 2017). No such campaign, as far as we know, exists for higher frequencies.

In this paper, we report results from a dedicated monitoring campaign of NGC 7469 with the single 30 m dish of the Institut de Radioastronomie Millimetrique (IRAM) at 95 GHz and at 143 GHz, simultaneous with *Swift*/XRT and *Swift*/UVOT monitoring that was part of a multi-wavelength campaign during the last part of 2015 (Behar et al. 2017). The IRAM observations were subsequently obtained to match, as closely as possible, the dense part of the *Swift*/XRT monitoring period.

2 OBSERVATIONS

2.1 NGC 7469

NGC 7469 is a nearby Seyfert galaxy at $z = 0.01588, D_L = 71.2$ Mpc, where $1''$ corresponds to $\approx$ 300 pc. It was observed many times with the VLA from 1.4 GHz up to 22 GHz (Unger et al. 1987; Lal et al. 2004; Orienti & Prieto 2010; Prouton et al. 2004), with the VLBI (Lonsdale et al. 1993, 2003) and with MERLIN (Thean et al. 2001). At 95 GHz it

Table 1. IRAM/EMIR bands used in this work.

Name	Lower bound (GHz)	Upper bound (GHz)
E090L	83	91
E090U	99	107
E150L	131	139
E150U	147	155
E090	E090L & E090U	
E150	E150L & E150U	

was observed with CARMA (Behar et al. 2015; Baldi et al. 2015), and at 350 GHz with ALMA (Izumi et al. 2015).

The high X-ray brightness and variability of NGC 7469 make it a popular target for X-ray telescopes, and in particular monitoring (e.g., Markowitz & Edelson 2004). In the visible too, NGC 7469 was monitored extensively, notable examples of which are its wavelength-dependent continuum delays of several light days, which indicate processing in an accretion disk (Collier et al. 1998), and reverberation mapping resulting in a black-hole mass measurement of $10^7 M_\odot$ (Peterson et al. 2014). In the following we describe the observations of our 2015 campaign.

2.2 mm-wave

NGC 7469 was monitored daily with the EMIR multi-band mm-wave receiver on the IRAM 30 m telescope from 2015, Nov 15 through 2015, Dec 31, except for 1 week at the end of November when an EMIR upgrade took place. Each observation included about 1 hr on source, which provides a sensitivity of typically 0.15 mK (0.8 mJy 1σ). In total, we obtained 36 flux measurements. The campaign yielded light curves in four EMIR bands (within B1 and B2, see Carter et al. 2012), each 8 GHz wide. These are listed in Table 1.

Antenna temperatures were obtained after subtracting the sky background measured by wobbling the secondary mirror at 2 Hz. To separate the effect of the optics between the two wobbler positions, we perform sub-scans with the source in one position of the wobbler, and then in the other position, and average the two. We then convert antenna temperature, after correction for atmospheric attenuation, to flux density using 6.2Jy/K at 86 GHz, 8.8Jy/K at 230 GHz, and a linear interpolation in between. We used Uranus as the flux calibrator. It was low on the horizon, and observed at 8.3 Jy.

In each band, we averaged over the two polarizations. Fig. 1 shows the four light curves in the four bottom panels. Although the photometric uncertainties are large (1σ = 0.8 mJy), in some cases there is inter-day variability of more than 1σ. We then also averaged each two adjacent bands to improve the Signal to Noise Ratio (S/N). The two averaged bands are (somewhat confusingly) named E090 centered around 95 GHz, and E150 centered around 143 GHz. Their light curves are shown in the two top panels with their smaller error bars, where inter-day variability can exceed 2σ.

The flux density of NGC 7469 at 95 GHz and at 143 GHz ranges between 6–14 mJy, and 4–13 mJy, respectively, which corresponds to $\nu L_\nu = (3.5 - 8.1) \times 10^{39}\,\mathrm{erg\,s^{-1}}$ at 95 GHz, and $\nu L_\nu = (3.5{-}11.3){\times}10^{39}\,\mathrm{erg\,s^{-1}}$ at 143 GHz. The present 95 GHz flux densities are marginally consistent with previous CARMA measurements, where the beam was much smaller. In the C configuration we measured 5.0 mJy in Nov 2013 (Behar et al. 2015), and 2–4 mJy (6–7 mJy in the D configuration) in Mar-Apr 2014 (Baldi et al. 2015). See Fig. 2 for a graphical comparison. The total- (as opposed to peak-) flux densities in 2014 are 6–11 mJy in the C configuration and 12–15 mJy in the D configuration (Baldi et al. 2015). The 30 m telescope has a beam size of $28''$ at 90 GHz and $17''$ at 150 GHz, while CARMA had a beam size at 95 GHz of $2\farcs2$ in the C configuration and $5\farcs5$ in the D configuration. The 1 kpc circumnuclear starburst ring of NGC 7469 is $2\farcs9$ across (Díaz-Santos et al. 2007). The reasonably good agreement between IRAM and CARMA, given also the variability, indicates the majority of the mm-wave flux comes from the AGN, and not from stars. Much below these length scales, however, any extended source beyond 1 light-month would dilute the variability signal from the core that we are after.

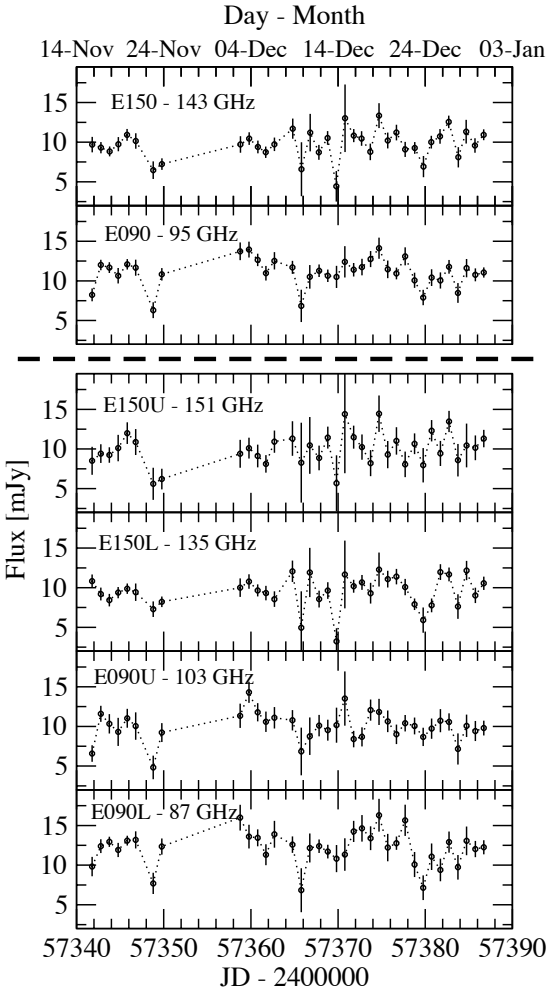


Figure 1. IRAM light curves in the four EMIR bands; central frequency is indicated for each (see Table 1 for details). The top two are co-added pairs from the bottom four. All panels span the same vertical range. Lines are drawn just to guide the eye.

2.3 Radio-mm SED

In Fig. 2 we plot the full radio-mm spectral energy distribution (SED) of NGC 7469, based mostly on archival measure-

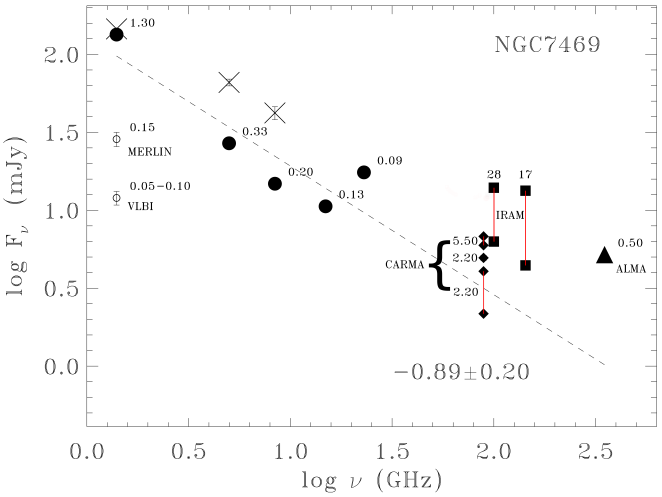


Figure 2. Radio to mm SED of NGC 7469. Numbers indicate beam size in arcseconds. VLA high-resolution data (A array) are plotted as full circles, lower resolution data (B-C-D arrays) as ×'s. Very high resolution data (MERLIN and VLBI) are shown with hollow circles. In the mm, present IRAM data are represented by squares, earlier CARMA data by diamonds; red lines indicate the range of variability in each campaign (see text). The ALMA measurement is the triangle. Fitting the A-array VLA data results in the dashed-line spectral slope of –0.89. IRAM, ALMA, and some CARMA points at $\gtrsim 90$ GHz fall above this slope, and may therefore represent a different AGN spectral component.

ments. Previous VLA observations were detailed in Behar et al. (2015). The present 95 GHz and 143 GHz data points (squares) can be seen to lie above the low-frequency steep slope of $\alpha = -0.89$. They are also much above the extrapolation from 350 GHz of the steep thermal dust emission in the far infrared (FIR) (Izumi et al. 2015).

At low radio frequencies, NGC 7469 is very bright, e.g., $F_{1.4\mathrm{GHz}} = 134$ mJy (Unger et al. 1987), which poses a concern of stellar contamination. The VLBI map of the inner region at 1.67 GHz shows several resolved and unresolved components associated with the AGN, each of order 10 mas (i.e., 3 pc) in size; the identification of the central AGN, however, is unclear (Lonsdale et al. 2003, Fig. 2 therein). Each of these point sources emits a few mJy for a total of ∼15 mJy in the central $\sim 0\farcs1$ (Lonsdale et al. 1993, 2003). VLBI apparently is insensitive to additional diffuse 15–20 mJy in that field, which MERLIN does detect within $\sim 0\farcs15$ (Thean et al. 2001; Lonsdale et al. 2003). Interestingly, these are also the scales of the strong X-ray outflow of NGC 7469, which is estimated to be around 30 pc or less (Peretz et al. 2018; Mehdipour et al. 2018). Thus, extended, optically-thin synchrotron emission is in fact expected from that region. If NGC 7469 varies at 95 GHz on time scales of days to weeks, as presently monitored, this mm component would be distinct from the low-frequency component, which seems to be the case, based on the SED (Fig. 2) as well.

At higher frequencies, $F_{350\mathrm{GHz}} = 5.19 \pm 0.09$ mJy was measured with ALMA from an unresolved $0\farcs5$ core (Izumi et al. 2015), which those authors conclude is due to thermal dust, because it is much above the extrapolated steep-slope power law. However, the 350 GHz flux may also contain a contribution from the optically thick mm-wave spectral component that is dominant at 100 GHz. Additionally, Izumi et al. (2015) measure an internal slope around 350 GHz of $\alpha = +2 \pm 1$, while dust would usually have $\alpha = 3.5$. Extrapolating this slope down to the present band of 90 – 150 GHz yields flux densities that are much below the measured 10 – 11 mJy, even for $\alpha = 1$.

A similar SED, with mm-wave excess above the low-frequency steep slope, and above the modeled dust from the FIR, is observed for another Seyfert galaxy NGC 3227 (Alonso-Herrero et al. 2019, Fig. 4 therein), whose ALMA observations show a rather complex structure of different spectral slopes $-1 < \alpha < +2$ between 230 – 350 GHz in the central few arcseconds (Fig. 3 therein). This likely indicates several components are contributing to the core emission, both in NGC 3227 and in NGC 7469.

2.4 *Swift*

During the entire mm-wave monitoring period, NGC 7469 was also observed daily for 1500 s with the X-ray Telescope (XRT) and the UV/Optical Telescope (UVOT) on board *Swift*. Exposures with each of the six UVOT filters are for 5 min. Data were reduced using xselect within the heasoft software package[1]. XRT was operated in PC mode. Source counts were extracted from a 20 pixel radius circle around the source and background from an annulus up to 30 pixels. XRT uncertainties are dominated by count statistics and are typically only a few percent. The light curves from all *Swift* instruments are presented in Fig. 3. The X-rays, measured between 0.3-10 keV can be seen to vary dramatically with no obvious trend, while the six UV/Optical light curves feature a rather uniform, slow and monotonous increase with time over the monitoring period.

2.5 *XMM-Newton Optical Monitor*

XMM-Newton observed NGC 7469 six times during the IRAM monitoring period. NGC 7469 varies in X-rays within hours, hence *XMM-Newton* probes much shorter time scales than we can currently monitor in the mm with IRAM. The *XMM-Newton* X-ray spectra were described in detail elsewhere (Behar et al. 2017; Peretz et al. 2018). Here, we focus on the *XMM-Newton* Optical Monitor (OM). The OM observed NGC 7469 for 4 ks with each of its six UV and optical filters, which are the same as those of *Swift*/UVOT. OM data were reduced using the XMM Science Analysis System (SAS) pipeline and the measurements are presented in Fig. 3 as red points. As expected, there is very good agreement between *Swift*/UVOT and *XMM-Newton*/OM in all filters.

2.6 *Wise Observatory*

Optical observations in Bessel V, R, and I filters were carried out with the 28″ Jay Baum Rich telescope at the Wise Observatory, Israel. An FLI ProLine PL16801 CCD was used as a detector with a pixel scale of 0.834 arcsec/pix. NGC 7469 was observed for 5 min in each filter once a night. On some nights several exposures were carried out in each filter and

[1] https://heasarc.gsfc.nasa.gov/lheasoft/

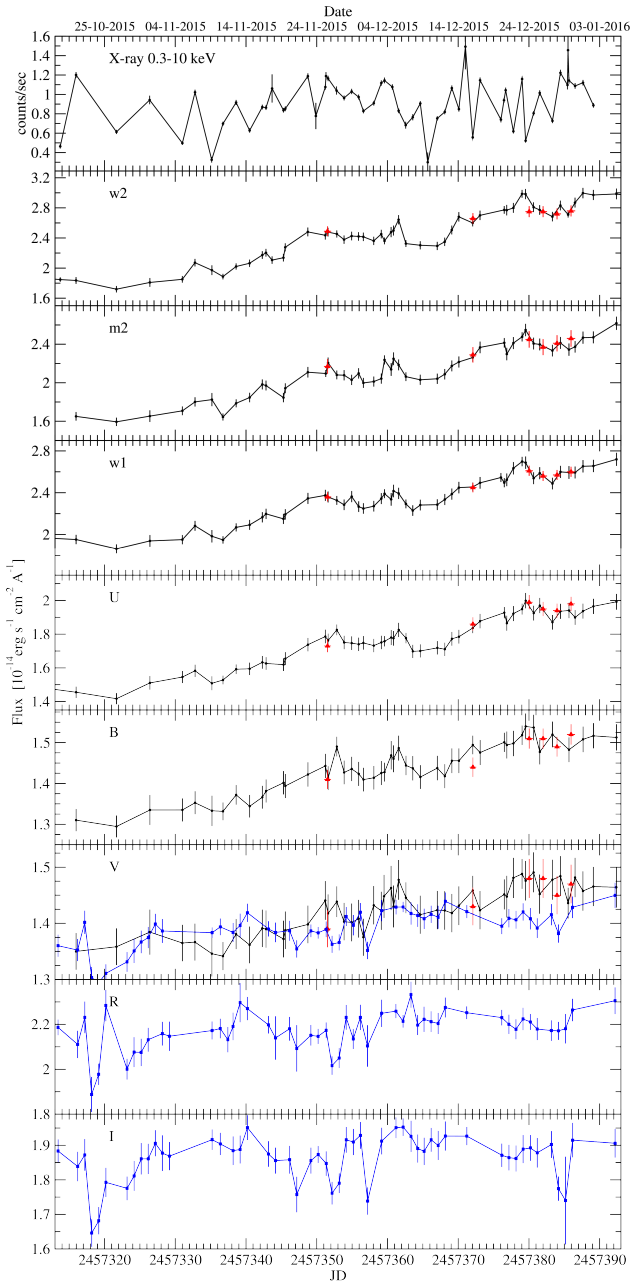


Figure 3. *Swift* light curves in X-rays and in six UV-optical bands (black points). Red triangles indicate (6) epochs measured with the *XMM-Newton* OM. Monitoring from the ground with the Wise Observatory is shown in the bottom three panels (blue squares). Lines are drawn just to guide the eye. All the data are listed in the appendix.

averaged into one data point per night. The data were reduced using standard IRAF[2] procedures. The broad-band light curves in the three filters are produced by comparing their instrumental magnitudes to those of constant-flux stars in the field (e.g., Netzer et al. 1996). Absolute photometry calibration was achieved by using stars with known magnitudes in the field of NGC 7469. The Wise light curves are shown in the three bottom panels of Fig. 3 with blue data points; the V band is over-plotted on the *Swift* OM V band, for comparison. We suspect these ground observations, when (slightly) discrepant from the space observations, are flawed due to atmospheric effects.

[2] IRAF (Image Reduction and Analysis Facility) is distributed by the National Optical Astronomy Observatories, which are operated by AURA, Inc, under cooperative agreement with the National Science Foundation.

3 RESULTS AND DISCUSSION

3.1 Variability

The summary of the variability parameters for the various light curves is given in Table 2. For each light curve we list the mean flux density $\langle F_\nu \rangle$ and its standard deviation STD. The χ^2 of the light curve with respect to a constant $\langle F_\nu \rangle$ is also listed. In the IRAM light curves there are $N = 36$ data points, hence $N - 1 = 35$ degrees of freedom for the reduced χ^2. The associated p-values, computed from χ^2 and the degrees of freedom, give an idea of the significance of the variability in each light curve, and can be thought of as the probability for no-variability, given the data and χ^2. These p-values in the IRAM light curves range from 10^{-7} to 0.1. The clearest indication of variability comes from the combined 95 GHz light curve E090. The least significant variability is in the E150U (151 GHz) light curve, but after combining with E150L, to give E150 (143 GHz), it indicates variability is highly likely ($p = 3 \times 10^{-5}$). Computing the various mm band correlations among themselves, yields nothing but a peak at zero, indicating this entire band, which we refer to loosely as the AGN mm-wave component, more or less varies together. The significance of the present variability is comparable and even higher (with twice as many data points) than that of the peak-flux light curve measured with CARMA (Baldi et al. 2015, see also Table 2 below), despite the order of magnitude disparity in beam size, which implies the dominant variability of the unresolved core.

The amplitude of variability in a light curve with N data points can be quantified with $F_{\rm var}$ (e.g. Edelson et al. 2002; Vaughan et al. 2003):

$$F_{\rm var} = \sqrt{\frac{STD^2 - \langle \sigma^2 \rangle}{\langle F_\nu \rangle^2}}, \quad (1)$$

and its uncertainty $\sigma_{F_{\rm var}}$

$$\sigma_{F_{\rm var}} = \sqrt{\left\{ \sqrt{\frac{\langle \sigma^2 \rangle}{N}} \cdot \frac{1}{\langle F_\nu \rangle} \right\}^2 + \left\{ \sqrt{\frac{1}{2N}} \cdot \frac{\langle \sigma^2 \rangle}{\langle F_\nu \rangle^2 F_{\rm var}} \right\}^2} \quad (2)$$

$F_{\rm var}$ represents the intrinsic variability amplitude in excess of the mean measurement uncertainty $\langle \sigma \rangle$. When the latter exceeds the former, $F_{\rm var}$ is not well defined, and a value of zero is given in Table 2. The $F_{\rm var}$ values of the combined light curves E090 and E150 over our 45 day IRAM campaign are both at the $13\% \pm 3\%$ level, very close to the previous CARMA results. $F_{\rm var}$ of the 0.3-10 keV X-ray light curve of *Swift*/XRT is twice as high at $25\% \pm 3\%$, but covers 75 days. For a better comparison with IRAM we therefore computed $F_{\rm var}$ for all *Swift*/XRT subsets of 45 days, and find $F_{\rm var} = 23\% - 26\%$ for all, so no difference from 75 days.

Markowitz & Edelson (2004) measured $F_{\rm var}$(2-12 keV) to be 16.0%±0.4% for NGC 7469 over 36 days using light

Table 2. Variability parameters of the various light curves of NGC 7469.

Light curve	N	ν	$\langle F_\nu \rangle$	STD	$F_{\rm var}$ (%)	$\frac{F_\nu^{\rm max}}{F_\nu^{\rm min}}$	χ^2	p-value
IRAM (Fig. 1)		(GHz)	(mJy)	(mJy)				
E150	36	143	9.7	1.9	12.6±3.4	3.0	78.6	3×10^{-5}
E090	36	95	11.1	1.8	12.9±2.4	2.2	96.9	10^{-7}
E150U	36	151	9.9	2.1	0 [1]	2.6	45.8	0.1
E150L	36	135	9.5	2.1	14.0±3.9	3.8	81.6	10^{-5}
E090U	36	103	10.0	1.8	9.7±4.1	3.0	56.5	0.01
E090L	36	87	12.1	2.2	13.5±2.9	2.4	66.7	10^{-3}
CARMA (Baldi et al. 2015)								
$F_\nu^{\rm peak}$	18	95	3.0	0.5	12.8±3.6	1.9	45.5	2×10^{-4}
$F_\nu^{\rm tot}$	18	95	8.1	1.0	7.4±3.5	1.6	22.4	0.17
Swift/XRT (Fig. 3)		$h\nu$ (keV)	(counts/s)	(counts/s)				
Total	57	0.3-10.0	0.91	0.23	25.0±2.6	5.0	3172.8	0
Hard	57	2.0-10.0	0.37	1.00	24.3±2.6	4.4	1746.9	0
Soft	57	0.3-2.0	0.54	0.16	28.4±2.9	5.7	2768.9	0
Hardness Ratio	57	···	$\langle HR \rangle = -0.17$	0.06	0 [1]	···	303.4	10^{-35}
Swift/UVOT (Fig. 3)		λ (Å)	(10^{-14}erg s^{-1}cm^{-2}Å^{-1})	(10^{-14}erg s^{-1}cm^{-2}Å^{-1})				
w2	54	1928	2.44	0.35	14±1.4	1.7	2651.9	0
m2	49	2246	2.12	0.26	12±1.3	1.6	1249.7	0
w1	53	2600	2.34	0.22	9.1±0.9	1.5	1045.0	0
U	52	3465	1.76	0.15	8.1±0.9	1.4	792.5	0
B	48	4392	1.43	0.06	3.9±0.5	1.2	235.7	6×10^{-27}
V	49	5468	1.42	0.04	1.8±0.5	1.1	80.7	2×10^{-3}
Wise (Fig. 3)								
V	51	5510	1.39	0.04	2.1±0.3	1.1	193.1	10^{-18}
R	52	6580	2.18	0.09	3±0.5	1.2	133.4	3×10^{-9}
I	52	8060	1.86	0.07	2.8±0.5	1.2	159.3	4×10^{-13}

[1]See text after Eq. 1.

Note. — The data of the light curves are listed in their entirety in the appendix.

curves from the RXTE telescope. We computed $F_{\rm var}$ for all present subsets of 36 days, which have at least 20 data points, and still get $F_{\rm var} = 22\% - 26\%$. Apparently in our *Swift*/XRT light curve, $F_{\rm var}$ is the same for any time scale between 30 - 70 days. This is consistent with Vagnetti et al. (2016, their Fig. 4), who found excess variance to vary slowly with light curve duration, as $t^{0.2}$. The higher $F_{\rm var}$ values in the present work than in Markowitz & Edelson (2004) are likely due to the more precise (lower $\langle \sigma^2 \rangle$) measurements of *Swift*/XRT, and to the stronger variability in the soft X-ray band. See Sec. 3.2 for more discussion on the hardness ratio.

Yet another measure of variability amplitude is the ratio of the highest $F_\nu^{\rm max}$ to lowest $F_\nu^{\rm min}$ flux density (Table 2). In the present IRAM data this ratio is between 2 and 4, while those of CARMA are less than 2 (Table 2). This may not be expected given the larger IRAM beam size, if there was appreciable extended emission, but evidently much of the emission is within a few arcseconds. The X-ray variability amplitude is even higher, reaching a factor of 5, while it is less than a factor 2 in the UV and down to 10% in the visible band. Interestingly, strong mm flux variability by a factor of 2 is observed within a day (Fig. 1). This suggests a 95 GHz source size of no more than 1 light day, which is just less than 10^{-3} pc, and which is approximately the physical size of the NGC 7469 core estimated from the luminosity of a self absorbed synchrotron source (Behar et al. 2015). These results call for intra-day mm-wave monitoring, and even better, coordinated mm-wave and X-ray monitoring on these shorter time scales.

Variability in the IR through the UV was measured in Seyferts many times, and specifically in NGC 7469. This variability for the most part is of small amplitude, as in Fig. 3, clearly distinct from that of the X-rays and the mm bands, which therefore likely arise from a different AGN component. Nonetheless, monitoring over many years reveals occasional significant drops in flux within months. Interestingly, in the IR the longest wavelengths (L band) vary most, and in the optical it is the shortest wavelengths (U band) (Glass 1998). This is likely because those arise from and gas closer in to the center, but the time scales imply it is still much farther away than the X-ray and mm sources.

3.2 X-ray Variability

Swift/XRT covers the broad energy band from 0.3 to 10.0 keV. It is beneficial to study the hard (2.0-10.0 keV) and soft (0.3-2.0 keV) bands separately, as they could come

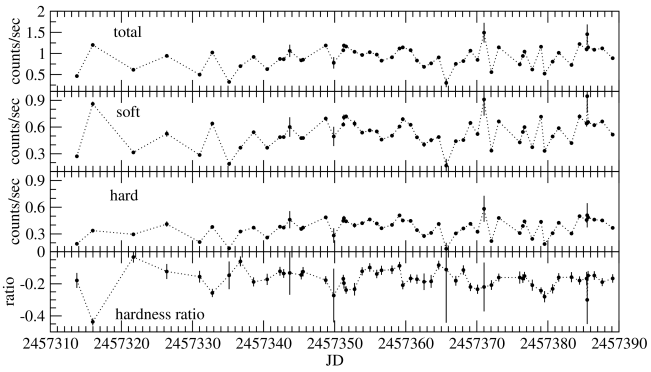


Figure 4. X-ray light curves of NGC 7469 in the hard (2.0-10.0 keV), soft (0.3-2.0 keV), and full bands. The light curve of the hardness ratio $HR = (H - S)/(H + S)$ is also plotted.

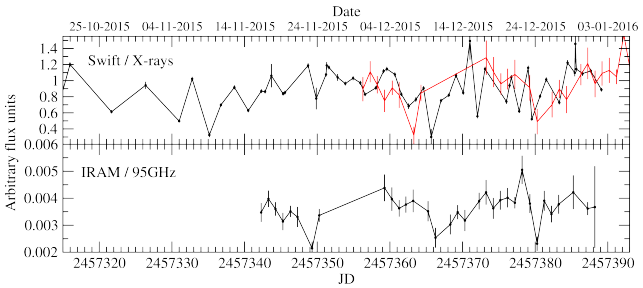


Figure 5. Light curves of NGC 7469 in X-rays (top) and 95 GHz (bottom). A tentative 14 day lag is demonstrated in the top panel by the red points, which are the (scaled) 95 GHz light curve shifted forward by 14 days.

from separate spectral components of the corona. The hardness of the spectrum can be an indication of the physical state of the source, and is therefore often also measured for its variability (McHardy et al. 1999, 2006; Peretz & Behar 2018). We denote here the hardness ratio in terms of *Swift*/XRT count rates (counts/s) $HR = (H - S)/(H + S)$, where H and S are the count rates in the hard and soft bands, respectively. Consequently, $-1 < HR < 1$. In Fig. 4, we present the *Swift*/XRT light curves in the two separate bands as well as that for HR. From inspection of Fig. 4 and Table 2 it can be seen that the soft band is slightly more variable.

X-ray variability can be caused by varying photoelectric absorption, rather than by genuine coronal variability. In that case, the source would become harder when dimmer (Mehdipour et al. 2017). This behaviour is not seen in the present case, where both bands vary relatively in unison, and HR varies relatively little.

Recently, Mehdipour & Costantini (2019) found in a sample of RL AGNs that radio loudness scales inversely with X-ray column density, so those sources are indeed more absorbed in X-rays (harder) when dimmer in the radio. Following that work, we checked for a correlation between the present E090 light curve (Fig. 1) and the X-ray hardness-ratio light curve (Fig. 4), which could be a proxy of absorption. We find only a weak correlation (Cross Correlation Coefficient $CCF \gtrsim 0.5$) at $t = 0$. If significant, this would indicate the mm-flux increases at the same time the X-rays become harder, which is opposite the effect of RL AGN (Mehdipour & Costantini 2019). In the context of a magnetic AGN corona, the correlation can be explained by freshly generated hot electrons. These electrons increase the synchrotron (mm) on one hand, and the most Compton boosted X-rays (hardness) on the other hand. However, such correlations and inferences need to await better short-temporal sampling of the mm and X-ray light curves.

3.3 The mm X-ray Connection

Among the IRAM light curves, E090 (95 GHz) shows the most robust variability. Hence, the E090 and X-ray light curves are compared in Fig. 5. The light curves are different, though the variability time scale of one-to-few days appears to be similar. In order to check for any time-lag between the two, we try to cross correlate the X-ray light curve with the mm one. No clear correlation is found, except a weak peak of $CCF = 0.6$ at -14 days. In the top panel of Fig. 5 we plot in red the 95 GHz light curve shifted forward by 14 days, on top of the X-ray one. It shows the gradual decrease in X-ray flux during the third week of December, followed by a gradual increase in the fourth week. The mm-wave light curve gives the sense of going through a similar transition two weeks earlier. Shorter time scales do not seem to correlate, but simultaneous monitoring on time scales of hours is required before any conclusive statement can be made.

The notion of radio/mm flares preceding X-ray flares can be associated with acceleration of fast electrons that emit synchrotron in the vicinity of magnetic fields, subsequently depositing their energy in the ambient medium, which then emits an X-ray flare. This is the scenario in some stellar coronal flares: Electrons accelerated through magnetic reconnection in the corona emit synchrotron radio, but X-rays are emitted only after they thermalize as they reach and evaporate the much denser chromosphere. In this scenario, only a small fraction of the energy is emitted in the radio/mm band. The vast majority is emitted eventually in X-rays, hence $L_{\rm X} \gg L_{\rm R}$.

Fig. 5 is only suggestive of such a connection in NGC 7469, but a time lag of a few days is interesting. In stellar coronae the lag between radio and X-rays can be ∼hours, which is by far longer than the coronal crossing time of ∼seconds, and not well understood. This means the electrons are trapped in the entangled coronal magnetic fields and diffuse slowly down to the chromosphere (for more details, see Güdel et al. 2002). Following through with the AGN analogy, if in NGC 7469 the lag is a few days and up to two weeks, the lifetime of fast electrons in the magnetic structures in the accretion disk corona would be about two orders of magnitude longer than they are in stellar coronae. If this is due to the size of the magnetic structures, scaling from stellar radii yields structures of 10^{13} cm, or in NGC 7469 a few gravitational radii, which is presumably the size of the X-ray corona. An important difference between stellar and AGN corona is the X-ray emitting processes. While in stellar corona the X-rays are emitted by thermal (10^6K) ions, in AGN X-rays are generated by (10^9K) electrons through Compton up-scattering of accretion-disk photons.

4 SUMMARY AND CONCLUSIONS

We monitored NGC 7469 at 95 GHz and at 143 GHz with the IRAM 30 m telescope over approximately a month and a half. The measured light curves indicate variability on time scales of days and less, similar to that detected before in NGC 7469 with CARMA (Baldi et al. 2015). The amplitude of variability is also similar in both campaigns, despite the much larger beam sizes in the present work, indicating the source is dominated by a small-size (light days) core.

In the present work, for the first time we measured an X-ray light curve simultaneous with the mm-wave ones. Both mm and X-ray sources vary on a similar time scale of days. This is in sharp contrast with the simultaneous UV-Optical light curves that slowly increased in flux in eight different filters during the course of the campaign, with no evident daily variability. This temporal behaviour constitutes clear evidence that the mm-wave source can be associated with the X-ray source (i.e., corona), but is distinct from the UV-Optical source (the accretion disk). The amplitude of variability over measurement uncertainties and its significance is somewhat higher in X-rays than in mm-waves, mostly due to the much more precise photometric measurements in X-rays. A tentative correlation between the mm and X-ray light curves suggests a ~ 14 day X-ray lag. If real, this lag could imply, by analogy to stellar coronae, that magnetically heated electrons produce the mm waves, and ultimately lose most of their energy by emitting X-rays.

Clearly, the present evidence for a temporal correlation, and for a true mm-wave flare preceding an X-ray one is only suggestive. Such a tentative connection between the mm-wave and X-ray sources, however, begs for more monitoring of nearby AGN, simultaneously in both bands. Since both the mm and the X-ray sources seem to vary on time scales which could be shorter than 1 day, it would be beneficial to monitor on both inter- and intra- day time scales. Such campaigns require higher sensitivity than that available with the IRAM 30 m telescope. Thus, higher-sensitivity (and resolution) arrays, e.g. ALMA, IRAM/NOEMA, and later SKA would be more suitable.

ACKNOWLEDGMENTS

This research is supported by the I-CORE program of the Planning and Budgeting Committee (grant 1937/12), and was performed in part at Aspen Center for Physics, which is supported by National Science Foundation grant PHY-1607611. We thank an anonymous referee for useful comments.

REFERENCES

Alonso-Herrero A., García-Burillo S., Pereira-Santaella M. S., et al. 2019, A&A, 628, A65
Anderson J. M., Ulvestad J. S., 2005, ApJ, 627, 674
Anderson J. M., Ulvestad J. S., Ho L. C., 2004, ApJ, 603, 42
Baldi R. D., Behar E., Laor A., Horesh A., 2015, MNRAS, 454, 4277
Barvainis R., Antonucci R., Coleman P., 1992, ApJ, 399, L19
Barvainis R., Lehár J., Birkinshaw M., Falcke H., Blundell K. M., 2005, ApJ, 618, 108
Behar E., Baldi R. D., Laor A., Horesh A., Stevens J., Tzioumis T., 2015, MNRAS, 451, 517
Behar E., Peretz U., Kriss G. A., Kaastra J., Arav N., Bianchi S., Branduardi-Raymont G., Cappi M., Costantini E., De Marco B., Di Gesu L., Ebrero J., Kaspi S., Mehdipour M., Paltani S., Petrucci P.-O., Ponti G., Ursini F., 2017, A&A, 601, A17
Behar E., Vogel S., Baldi R. D., Smith K. L., Mushotzky R. F., 2018, MNRAS, 478, 399
Bell M. E., Tzioumis T., Uttley P., Fender R. P., Arévalo P., Breedt E., McHardy I., Calvelo D. E., Jamil O., Körding E., 2011, MNRAS, 411, 402
Carter M., Lazareff B., Maier D., Chenu J.-Y., Fontana A.-L., Bortolotti Y., Boucher C., Navarrini A., Blanchet S., Greve A., John D., Kramer C., Morel F., Navarro S., Peñalver J., Schuster K. F., Thum C., 2012, A&A, 538, A89
Collier S. J., Horne K., Kaspi S., et al. 1998, ApJ, 500, 162
Díaz-Santos T., Alonso-Herrero A., Colina L., Ryder S. D., Knapen J. H., 2007, ApJ, 661, 149
Doi A., Kameno S., Kohno K., Nakanishi K., Inoue M., 2005, MNRAS, 363, 692
Doi A., Nakanishi K., Nagai H., Kohno K., Kameno S., 2011, AJ, 142, 167
Edelson R., Turner T. J., Pounds K., Vaughan S., Markowitz A., Marshall H., Dobbie P., Warwick R., 2002, ApJ, 568, 610
Falcke H., Lehár J., Barvainis R., Nagar N. M., Wilson A. S., 2001, in Peterson B. M., Pogge R. W., Polidan R. S., eds, Probing the Physics of Active Galactic Nuclei Vol. 224 of Astronomical Society of the Pacific Conference Series, Radio Variability in Radio-Quiet Quasars and Low-Luminosity AGN. p. 265
Field G. B., Rogers R. D., 1993, ApJ, 403, 94
Glass I. S., 1998, MNRAS, 297, 18
Güdel M., Audard M., Smith K. W., Behar E., Beasley A. J., Mewe R., 2002, ApJ, 577, 371
Güdel M., Benz A. O., 1993, ApJ, 405, L63
Ho L. C., Peng C. Y., 2001, ApJ, 555, 650
Hughes D. H., Robson E. I., Dunlop J. S., Gear W. K., 1993, MNRAS, 263, 607
Inoue Y., Doi A., 2014, PASJ, 66, L8
Inoue Y., Doi A., 2018, ApJ, 869, 114
Izumi T., Kohno K., Aalto S., et al. 2015, ApJ, 811, 39
Jones S., McHardy I., Maccarone T. J., 2017, MNRAS, 465, 1336
Lal D. V., Shastri P., Gabuzda D. C., 2004, A&A, 425, 99
Laor A., Baldi R. D., Behar E., 2019, MNRAS, 482, 5513
Laor A., Behar E., 2008, MNRAS, 390, 847
Lonsdale C. J., Lonsdale C. J., Smith H. E., Diamond P. J., 2003, ApJ, 592, 804
Lonsdale C. J., Smith H. J., Lonsdale C. J., 1993, ApJ, 405, L9
Markowitz A., Edelson R., 2004, ApJ, 617, 939
McHardy I. M., Koerding E., Knigge C., Uttley P., Fender R. P., 2006, Nature, 444, 730
McHardy I. M., Papadakis I. E., Uttley P., 1999, Nuclear Physics B Proceedings Supplements, 69, 509
Mehdipour M., Costantini E., 2019, Astronomy and Astrophysics, 625, A25

Mehdipour M., Kaastra J. S., Costantini E., Behar E., Kriss G. A., Bianchi S., Brand uardi-Raymont G., Cappi M., Ebrero J., Di Gesu L., Kaspi S., Mao J., De Marco B., Middei R., Peretz U., Petrucci P. O., Ponti G., Ursini F., 2018, A&A, 615, A72
Mehdipour M., Kaastra J. S., Kriss G. A., et al. 2017, Astronomy and Astrophysics, 607, A28
Mundell C. G., Ferruit P., Nagar N., Wilson A. S., 2009, ApJ, 703, 802
Neff S. G., de Bruyn A. G., 1983, A&A, 128, 318
Netzer H., Heller A., Loinger F., Alexand er T., Baldwin J. A., Wills B. J., Han M., Frueh M., Higdon J. L., 1996, MNRAS, 279, 429
Orienti M., Prieto M. A., 2010, MNRAS, 401, 2599
Panessa F., Baldi R. D., Laor A., Padovani P., Behar E., McHardy I., 2019, Nature Astronomy, 3, 387
Peretz U., Behar E., 2018, Monthly Notices of the Royal Astronomical Society, 481, 3563
Peretz U., Behar E., Kriss G. A., Kaastra J., Arav N., Bianchi S., Branduardi-Raymont G., Cappi M., Costantini E., De Marco B., 2018, A&A, 609, A35
Pérez-Torres M. A., Alberdi A., Colina L., Torrelles J. M., Panagia N., Wilson A., Kankare E., Mattila S., 2009, MNRAS, 399, 1641
Peterson B. M., Grier C. J., Horne K., et al. 2014, ApJ, 795, 149
Prouton O. R., Bressan A., Clemens M., Franceschini A., Granato G. L., Silva L., 2004, A&A, 421, 115
Raginski I., Laor A., 2016, MNRAS, 459, 2082
Schmidt M., Green R. F., 1983, ApJ, 269, 352
Thean A. H. C., Gillibrand T. I., Pedlar A., Kukula M. J., 2001, MNRAS, 327, 369
Ulvestad J. S., Antonucci R. R. J., Barvainis R., 2005, ApJ, 621, 123
Unger S. W., Lawrence A., Wilson A. S., Elvis M., Wright A. E., 1987, MNRAS, 228, 521
Vagnetti F., Middei R., Antonucci M., Paolillo M., Serafinelli R., 2016, A&A, 593, A55
Vaughan S., Edelson R., Warwick R. S., Uttley P., 2003, MNRAS, 345, 1271
Wrobel J. M., 2000, ApJ, 531, 716

APPENDIX A: LIGHT CURVE DATA

The complete data sets of the present monitoring campaign are listed below.

Table A1. *Swift* light curves. XRT measurements are in counts/s. All UVOT flux densities F_λ are in 10^{-14}erg s^{-1} cm^{-2}Å^{-1}. JD is listed as JD-2457300.

Swift													
XRT		w2		m2		w1		U		B		V	
JD	counts/s	JD	F_λ	JD	F_λ	JD	F_λ	JD	F_λ	JD	F_λ	JD	F_λ
13.740	0.464±0.022	13.741	1.848±0.029	15.974	1.651±0.045	15.976	1.952±0.045	15.979	1.455±0.034	15.982	1.310±0.027	15.971	1.350±0.033
15.975	1.201±0.029	15.968	1.836±0.045	21.686	1.594±0.043	21.689	1.862±0.043	21.692	1.417±0.033	21.695	1.295±0.027	21.683	1.358±0.033
21.687	0.613±0.021	21.681	1.720±0.042	26.413	1.653±0.060	26.414	1.938±0.056	26.415	1.511±0.041	26.416	1.335±0.037	26.412	1.384±0.040
26.382	0.942±0.044	26.411	1.810±0.058	31.003	1.708±0.045	31.006	1.950±0.044	31.009	1.546±0.036	31.012	1.335±0.028	31.000	1.365±0.033
31.004	0.498±0.018	30.997	1.851±0.045	32.793	1.801±0.048	32.796	2.083±0.047	32.799	1.583±0.037	32.802	1.353±0.028	32.790	1.367±0.033
32.794	1.022±0.027	32.787	2.072±0.050	35.181	1.825±0.068	35.182	1.983±0.059	35.182	1.508±0.042	35.183	1.333±0.037	35.180	1.346±0.041
35.152	0.325±0.029	35.179	1.972±0.065	36.744	1.644±0.037	36.746	1.948±0.035	36.747	1.528±0.027	36.749	1.332±0.022	36.742	1.342±0.025
36.745	0.698±0.021	36.741	1.887±0.037	38.604	1.786±0.041	38.606	2.068±0.039	38.607	1.592±0.029	38.608	1.372±0.024	38.603	1.381±0.027
38.603	0.917±0.026	38.601	2.021±0.041	40.509	1.847±0.049	40.512	2.092±0.047	40.514	1.594±0.037	40.517	1.344±0.028	40.506	1.362±0.033
40.511	0.628±0.022	40.503	2.064±0.049	42.305	1.982±0.052	42.308	2.165±0.049	42.311	1.633±0.038	42.314	1.366±0.028	42.302	1.391±0.033
42.306	0.870±0.024	42.299	2.173±0.051	42.830	1.971±0.051	42.833	2.197±0.049	42.836	1.626±0.038	42.839	1.381±0.029	42.827	1.390±0.033
42.831	0.863±0.024	42.824	2.204±0.052	45.297	1.846±0.048	45.300	2.150±0.048	45.303	1.619±0.038	45.306	1.402±0.029	45.294	1.372±0.033
43.687	1.061±0.146	43.688	2.107±0.050	45.557	1.943±0.051	45.559	2.192±0.050	45.562	1.655±0.039	45.565	1.394±0.029	45.554	1.388±0.034
45.298	0.837±0.023	45.291	2.138±0.050	48.750	2.109±0.055	48.752	2.345±0.053	48.755	1.738±0.040	48.758	1.422±0.030	48.747	1.398±0.034
45.558	0.852±0.025	45.551	2.276±0.054	51.276	2.096±0.036	51.218	2.375±0.053	51.221	1.786±0.041	51.224	1.443±0.030	51.212	1.441±0.034
48.751	1.188±0.029	48.744	2.481±0.058	51.606	2.206±0.056	51.609	2.359±0.053	51.612	1.763±0.041	51.615	1.413±0.029	51.603	1.418±0.034
49.873	0.777±0.135	51.208	2.435±0.057	52.839	2.081±0.046	52.841	2.326±0.042	52.842	1.826±0.032	52.843	1.490±0.024	52.838	1.439±0.027
51.216	1.076±0.027	51.600	2.478±0.058	53.867	2.078±0.053	53.870	2.284±0.051	53.873	1.751±0.040	53.876	1.427±0.029	53.864	1.403±0.034
51.305	1.189±0.041	52.837	2.454±0.047	54.937	2.030±0.053	54.940	2.363±0.053	54.943	1.747±0.041	54.945	1.436±0.030	54.934	1.402±0.034
51.607	1.165±0.028	53.861	2.378±0.055	55.927	2.097±0.054	55.930	2.266±0.051	55.933	1.740±0.040	55.936	1.424±0.029	55.924	1.408±0.034
52.803	1.040±0.042	54.931	2.426±0.057	56.592	1.998±0.052	56.596	2.249±0.050	56.599	1.748±0.040	56.601	1.410±0.029	56.589	1.375±0.033
53.868	0.963±0.025	55.921	2.421±0.056	58.063	2.012±0.052	58.066	2.271±0.051	58.069	1.732±0.040	58.072	1.414±0.029	58.060	1.432±0.034
54.938	1.030±0.027	56.586	2.416±0.056	59.124	2.043±0.053	59.127	2.343±0.052	59.130	1.751±0.041	59.133	1.426±0.029	59.120	1.422±0.034
55.929	0.973±0.026	58.057	2.362±0.055	59.585	2.237±0.047	59.587	2.390±0.042	59.588	1.758±0.031	59.590	1.428±0.023	59.517	1.448±0.038
56.594	0.828±0.024	59.117	2.452±0.057	60.517	2.138±0.066	60.518	2.336±0.060	60.519	1.780±0.045	60.520	1.469±0.035	60.515	1.463±0.040
58.064	0.909±0.024	59.583	2.361±0.045	60.854	2.249±0.066	60.855	2.416±0.060	60.857	1.775±0.044	60.858	1.460±0.033	60.852	1.430±0.038
59.125	1.117±0.027	60.514	2.478±0.068	61.579	2.185±0.056	61.582	2.393±0.054	61.585	1.826±0.042	61.588	1.487±0.031	61.576	1.477±0.035
59.586	1.144±0.029	60.851	2.499±0.066	62.610	2.063±0.046	62.611	2.293±0.042	62.612	1.777±0.032	62.614	1.444±0.024	62.608	1.446±0.028
60.686	1.077±0.028	61.573	2.643±0.061	64.637	2.031±0.053	63.577	2.229±0.050	63.579	1.698±0.040	63.582	1.437±0.030	64.634	1.415±0.034
61.580	0.831±0.024	62.607	2.326±0.046	67.042	2.041±0.053	64.640	2.282±0.051	64.643	1.700±0.039	64.646	1.416±0.029	67.039	1.423±0.034
62.578	0.683±0.036	64.631	2.303±0.054	68.103	2.088±0.054	67.045	2.286±0.051	67.048	1.719±0.040	67.050	1.438±0.030	68.100	1.423±0.034
63.575	0.765±0.031	67.036	2.294±0.054	69.100	2.175±0.056	68.106	2.335±0.052	68.108	1.711±0.040	68.111	1.418±0.029	69.097	1.418±0.034
64.639	0.907±0.024	68.097	2.350±0.056	70.097	2.216±0.057	69.102	2.387±0.054	69.105	1.772±0.041	69.108	1.456±0.030	70.094	1.431±0.035
65.695	0.300±0.100	69.094	2.506±0.059	72.054	2.262±0.044	70.100	2.449±0.055	70.102	1.785±0.042	70.105	1.456±0.030	72.052	1.459±0.026
67.043	0.753±0.023	70.091	2.682±0.062	73.088	2.367±0.060	72.055	2.455±0.041	72.057	1.836±0.031	72.059	1.494±0.023	73.085	1.423±0.034
68.104	0.819±0.024	72.050	2.600±0.046	76.512	2.415±0.049	73.091	2.494±0.056	73.094	1.877±0.044	73.097	1.476±0.031	76.510	1.451±0.027
69.101	1.065±0.027	73.082	2.701±0.063	76.870	2.298±0.065	76.040	2.546±0.043	76.516	1.927±0.034	76.518	1.501±0.024	76.868	1.448±0.037
70.098	0.848±0.025	76.508	2.773±0.051	77.802	2.412±0.062	76.514	2.496±0.044	76.873	1.865±0.045	76.875	1.494±0.033	77.799	1.481±0.036
71.017	1.493±0.233	76.866	2.769±0.070	79.032	2.477±0.048	76.872	2.524±0.061	77.807	1.922±0.045	77.810	1.498±0.031	79.030	1.488±0.027
72.054	0.557±0.017	77.797	2.800±0.065	79.531	2.548±0.064	77.805	2.634±0.059	79.036	1.949±0.033	79.038	1.518±0.024	79.528	1.476±0.035
73.089	1.146±0.028	79.028	2.987±0.052	80.664	2.407±0.061	79.034	2.698±0.045	79.537	1.999±0.046	79.540	1.540±0.032	80.661	1.491±0.036
76.042	0.740±0.028	79.525	2.983±0.068	81.525	2.398±0.061	79.534	2.688±0.059	80.669	1.925±0.045	80.672	1.537±0.032	81.522	1.452±0.035
76.477	0.940±0.025	80.658	2.809±0.065	83.319	2.334±0.060	80.666	2.539±0.057	81.530	1.970±0.046	81.533	1.477±0.031	83.316	1.478±0.036
76.711	1.043±0.027	81.519	2.772±0.064	84.453	2.413±0.061	81.527	2.587±0.058	83.325	1.870±0.044	83.327	1.520±0.032	84.450	1.484±0.036
77.803	0.619±0.022	83.314	2.684±0.063	85.656	2.344±0.064	83.322	2.488±0.056	84.459	1.936±0.045	85.663	1.483±0.031	85.543	1.436±0.028
79.033	1.159±0.025	84.447	2.832±0.065	86.521	2.373±0.060	84.456	2.599±0.058	85.660	1.941±0.046	87.650	1.508±0.032	86.518	1.482±0.035
79.533	0.523±0.019	85.541	2.710±0.039	87.641	2.468±0.063	85.658	2.594±0.061	86.527	1.899±0.044	89.119	1.517±0.031	87.638	1.458±0.035
80.665	0.806±0.024	86.515	2.870±0.065	89.110	2.471±0.062	86.524	2.594±0.057	87.647	1.937±0.045	92.377	1.513±0.032	89.107	1.466±0.035
81.526	1.015±0.027	87.636	2.996±0.069	92.371	2.618±0.069	87.644	2.653±0.059	89.116	1.965±0.045			92.369	1.464±0.036
83.320	0.727±0.023	89.104	2.972±0.067			89.113	2.656±0.058	92.375	1.992±0.047				
84.453	1.222±0.032	92.366	2.985±0.071			92.373	2.719±0.062						
85.447	1.097±0.046												
85.524	1.456±0.230												
85.657	1.143±0.033												
86.521	1.087±0.029												
87.642	1.121±0.029												
89.111	0.887±0.024												

Table A2. Wise and mm-wave light curves. Flux density F_λ in the optical is given in 10^{-14}erg s^{-1} cm^{-2}Å^{-1}. Flux density F_ν in the mm is given in mJy. JD is listed as JD-2457300.

Optical						mm			
V		R		I		E090		E150	
JD	F_λ	JD	F_λ	JD	F_λ	JD	F_ν	JD	F_ν
13.429	1.360±0.020	13.424	2.187±0.036	13.433	1.884±0.034	41.785	8.24±0.81	41.785	9.69±0.97
16.203	1.352±0.020	16.198	2.111±0.061	16.207	1.839±0.043	42.785	12.01±0.67	42.785	9.31±0.71
17.200	1.402±0.021	17.213	2.231±0.071	17.204	1.872±0.046	43.762	11.67±0.68	43.762	8.83±0.63
18.181	1.303±0.019	18.177	1.888±0.078	18.185	1.646±0.040	44.777	10.65±0.98	44.777	9.74±0.89
19.179	1.294±0.021	19.174	1.978±0.048	19.183	1.681±0.040	45.820	12.09±0.66	45.820	10.92±0.75
20.188	1.311±0.016	20.183	2.284±0.070	20.192	1.793±0.042	46.781	11.66±1.01	46.781	10.15±0.98
23.183	1.331±0.018	23.179	2.000±0.047	23.188	1.775±0.034	48.797	6.30±1.00	48.797	6.47±1.11
24.178	1.351±0.022	24.173	2.076±0.067	24.182	1.811±0.043	49.781	10.83±0.78	49.781	7.23±0.72
25.177	1.367±0.020	25.172	2.075±0.061	25.181	1.861±0.046	58.770	13.73±1.12	58.770	9.71±1.05
26.176	1.375±0.019	26.172	2.132±0.053	26.181	1.861±0.044	59.777	13.95±1.00	59.777	10.46±0.80
27.176	1.399±0.018	28.171	2.159±0.053	27.181	1.906±0.038	60.777	12.64±0.78	60.777	9.39±0.80
28.175	1.386±0.021	29.173	2.147±0.065	28.179	1.877±0.052	61.719	10.97±0.92	61.719	8.73±0.71
35.207	1.383±0.009	35.202	2.173±0.041	29.182	1.869±0.041	62.703	12.53±1.09	62.703	9.72±0.85
36.365	1.394±0.015	36.361	2.182±0.044	35.211	1.916±0.030	64.770	11.71±0.82	64.770	11.70±1.27
38.169	1.384±0.017	37.434	2.132±0.057	36.370	1.904±0.032	65.777	6.85±2.04	65.777	6.59±3.40
39.168	1.396±0.021	38.165	2.191±0.062	38.174	1.884±0.042	66.758	10.51±1.49	66.758	11.20±2.37
40.199	1.419±0.016	39.163	2.297±0.087	39.172	1.888±0.041	67.820	11.28±0.79	67.820	8.72±0.93
43.177	1.390±0.014	40.194	2.270±0.052	40.203	1.951±0.036	68.820	10.65±0.78	68.820	10.53±0.86
44.179	1.384±0.018	43.173	2.198±0.039	43.181	1.875±0.037	69.828	10.51±1.39	69.828	4.43±1.93
46.170	1.387±0.018	44.175	2.140±0.097	44.174	1.856±0.038	70.781	12.41±1.98	70.781	13.02±4.26
47.172	1.354±0.015	46.166	2.180±0.053	46.174	1.858±0.040	71.785	11.40±0.85	71.785	10.83±0.82
49.176	1.387±0.011	47.174	2.093±0.104	47.183	1.758±0.052	72.738	11.74±1.04	72.738	10.46±0.92
50.197	1.383±0.011	49.171	2.151±0.046	49.180	1.856±0.038	73.734	12.75±1.01	73.734	8.77±1.04
51.333	1.389±0.014	50.192	2.147±0.034	50.201	1.873±0.024	74.699	14.12±1.33	74.699	13.35±1.57
52.166	1.363±0.015	51.329	2.174±0.036	51.337	1.847±0.036	75.695	11.45±1.11	75.695	10.21±1.00
53.174	1.366±0.015	52.162	2.016±0.041	52.171	1.761±0.033	76.699	10.94±0.74	76.699	11.21±0.99
54.165	1.412±0.017	53.170	2.050±0.045	53.179	1.790±0.029	77.699	13.10±1.13	77.699	9.09±0.95
55.168	1.397±0.018	54.161	2.231±0.055	54.170	1.916±0.037	78.773	10.08±0.96	78.773	9.27±0.74
56.170	1.420±0.016	55.164	2.135±0.045	55.173	1.909±0.038	79.766	7.90±0.97	79.766	6.92±1.34
57.191	1.352±0.016	56.166	2.231±0.057	56.174	1.929±0.039	80.734	10.41±1.06	80.734	10.00±0.80
59.180	1.423±0.019	57.174	2.104±0.093	57.195	1.739±0.040	81.738	10.05±1.02	81.738	10.73±0.93
61.208	1.429±0.013	59.176	2.249±0.061	59.184	1.912±0.039	82.734	11.77±0.86	82.734	12.56±0.79
62.209	1.429±0.009	61.200	2.259±0.032	61.209	1.951±0.030	83.750	8.48±1.25	83.750	8.10±1.28
63.329	1.417±0.020	62.205	2.214±0.029	62.214	1.953±0.025	84.742	11.61±1.16	84.742	11.32±1.49
64.276	1.414±0.020	63.325	2.332±0.058	63.333	1.926±0.045	85.746	10.76±0.81	85.746	9.58±0.91
65.177	1.408±0.018	64.272	2.197±0.045	64.280	1.891±0.041	86.715	11.06±0.64	86.715	10.93±0.69
66.169	1.416±0.015	65.172	2.223±0.056	65.181	1.883±0.040				
67.168	1.411±0.021	66.165	2.212±0.046	66.174	1.916±0.035				
68.176	1.439±0.016	67.163	2.204±0.047	67.172	1.900±0.042				
71.218	1.421±0.012	68.172	2.275±0.045	68.181	1.927±0.042				
76.168	1.395±0.014	71.211	2.252±0.028	71.220	1.927±0.027				
77.169	1.409±0.016	76.164	2.230±0.035	76.173	1.871±0.034				
78.172	1.406±0.016	77.165	2.200±0.043	77.173	1.864±0.037				
79.168	1.420±0.016	78.168	2.178±0.045	78.177	1.862±0.038				
80.204	1.408±0.019	79.164	2.224±0.050	79.173	1.889±0.041				
81.174	1.391±0.018	80.200	2.211±0.036	80.208	1.892±0.037				
83.172	1.415±0.019	81.169	2.179±0.050	81.178	1.878±0.043				
84.172	1.382±0.016	83.168	2.172±0.046	83.176	1.902±0.039				
85.172	1.313±0.060	84.167	2.171±0.040	84.176	1.775±0.035				
86.173	1.429±0.019	85.168	2.180±0.066	85.177	1.740±0.127				
92.180	1.450±0.023	86.169	2.264±0.051	86.177	1.915±0.050				
		92.176	2.305±0.060	92.185	1.906±0.042				

Table A3. *XMM-Newton*/OM light curves. Flux density F_λ is given in 10^{-14}erg s^{-1}cm^{-2} Å^{-1}. JD is listed as JD-2457300.

	XMM-Newton/OM					
JD	w2	m2	w1	U	B	V
	F_λ	F_λ	F_λ	F_λ	F_λ	F_λ
51.527	2.490±0.065	2.170±0.076	2.360±0.044	1.730±0.038	1.410±0.023	1.390±0.033
72.084	2.660±0.070	2.290±0.080	2.450±0.046	1.860±0.041	1.440±0.024	1.430±0.034
80.030	2.750±0.073	2.450±0.086	2.610±0.049	1.990±0.043	1.510±0.025	1.480±0.035
82.001	2.750±0.073	2.370±0.083	2.560±0.048	1.950±0.042	1.510±0.025	1.480±0.035
83.966	2.720±0.072	2.410±0.084	2.570±0.048	1.940±0.042	1.490±0.025	1.450±0.034
85.950	2.760±0.073	2.460±0.086	2.600±0.049	1.980±0.043	1.520±0.025	1.470±0.035